Journal of Computational Physics **165,** 69–88 (2000)
doi:10.1006/jcph.2000.6597, available online at http://www.idealibrary.com on IDEAL®

A High-Order Gas-Kinetic Method for Multidimensional Ideal Magnetohydrodynamics

Hua-Zhong Tang* and Kun Xu†

**State Key Laboratory of Scientific and Engineering Computing, Institute of Computational Mathematics, Chinese Academy of Sciences, Beijing 100080, China; and †Department of Mathematics, The Hong Kong University of Science and Technology, Clear Water Bay, Kowloon, Hong Kong*
E-mail: makxu@uxmail.ust.hk

Received October 25, 1999; revised February 28, 2000; published online November 3, 2000

This paper extends the gas-kinetic theory based flux splitting method for ideal magnetohydrodynamics (MHD) equations (K. Xu, 1999, *J. Comput. Phys.* **153**, 334) to multidimensional cases. The kinetic MHD scheme is constructed based on the direct splitting of the macroscopic flux functions with the consideration of particle transport. At the same time, particle "collisions" are implemented in the free transport process to reduce the numerical dissipation. The high-order resolution of the scheme is achieved through the MUSCL-type initial reconstruction and the Runge–Kutta time-stepping method. The numerical tests include the spherical explosion, the Kelvin–Helmholtz instability, and the Orszag–Tang MHD turbulence problems. Numerical results validate the accuracy of the kinetic approach. © 2000 Academic Press

Key Words: magnetohydrodynamics; kinetic method.

---

1. INTRODUCTION

The multidimensional ideal MHD equations are

$$\begin{aligned}
\rho_t + \nabla\cdot(\rho\mathbf{u}) &= 0,\\
(\rho\mathbf{u})_t + \nabla\cdot\left[\rho\mathbf{u}\mathbf{u} + \left(p+\frac{1}{2}B^2\right)I - \mathbf{B}\mathbf{B}\right] &= 0,\\
\mathbf{B}_t - \nabla\times(\mathbf{u}\times\mathbf{B}) &= 0,\\
(E)_t + \nabla\cdot\left[\mathbf{u}(E+p) - (\mathbf{u}\times\mathbf{B})\times\mathbf{B}\right] &= 0,
\end{aligned}\tag{1.1}$$

where ρ, p, $\mathbf{u} = (u_x, u_y, u_z)$, and $\mathbf{B} = (B_x, B_y, B_z)$ denote mass density, gas pressure, fluid velocity vector, and magnetic field, respectively. The total energy density includes thermal,

0021-9991/00 $35.00

kinetic, and magnetic energies,

$$E = \rho e + \frac{1}{2}(\rho u^2 + B^2), \tag{1.2}$$

where ρe is the thermal energy density, $u^2 = u_x^2 + u_y^2 + u_z^2$, and $B^2 = B_x^2 + B_y^2 + B_z^2$. For ideal gases, the thermal energy is related to the gas pressure through the relation

$$p = (\gamma - 1)\rho e, \tag{1.3}$$

where γ is the ratio of the specific heats. In addition to these equations, the magnetic field has to satisfy the divergence-free condition; i.e., $\nabla \cdot \mathbf{B} = 0$.

In the past decade, various high-resolution schemes have been developed for the MHD equations. Most of these schemes are based on the approximate Riemann solvers [1, 3, 5, 8, 9, 13, 16, 21, 27], where seven- or eight-wave family eigensystems are used in the characteristic decomposition. Due to the nonstrict hyperbolicity of the MHD system, considerable work is required for the validation of the MHD eigensystem. Recently, based on the particle transport mechanism, Croisille *et al.* and Xu constructed gas-kinetic MHD solvers [6, 26]. Because of the simplicity of the kinetic flux functions, the efficiency becomes one of the advantages in the kinetic approach. In the current paper, the accuracy of the kinetic method will be further demonstrated in the multidimensional cases.

The accuracy and robustness of any shock-capturing scheme depend on how smart the introduction of the numerical dissipation is. There are two sources of the numerical dissipations introduced in the MUSCL-type shock-capturing schemes. One is from the initial reconstruction, and the other is from the underlying dynamics of the gas evolution model. For the flux vector splitting (FVS) schemes [14, 19, 23], the splitting of the flux function to $F = F^+ + F^-$ assumes the particle or wave-free transport mechanism, which implicitly sets the particle mean free path equal to the cell size. Therefore, the numerical viscosity coefficient in the FVS model will be proportional to the cell size Δx; i.e., $\nu_{\text{num}} \sim \Delta x$ [25]. For high-resolution methods, the dissipation is much reduced due to the reconstruction of initial data. For example, in the smooth flow region, a second-order scheme should have theoretically $\nu_{\text{num}} \sim (\Delta x)^2$. Besides the high-order initial interpolation, the introduction of particle collisions in the gas evolution stage is still necessary to reduce the numerical dissipation [26].

The current paper extends the gas-kinetic theory based flux splitting MHD method [26] to high-order and multidimensions. Similarly to many other schemes, a directional splitting method is used to update flow variables. High-order spatial resolution is obtained using a MUSCL-type reconstruction technique, and temporal accuracy is achieved through the Runge–Kutta method. Also, in order to impose the divergence-free condition for the magnetic field $\nabla \cdot \mathbf{B} = 0$, a correction method is enforced in solving the Possion equation for the potential ϕ, such as $\nabla^2\phi + \nabla \cdot \mathbf{B} = 0$, to obtain the corrected magnetic field $\mathbf{B}^{\text{c}}$ through $\mathbf{B}^{\text{c}} = \mathbf{B} + \nabla\phi$, where $\nabla \cdot \mathbf{B}^{\text{c}} = 0$ is satisfied. This technique is used in many MHD solvers [4, 9, 27]. The current method has only second-order accuracy in the smooth flow region. It may not be suitable for problems with very long time simulation involving complicated waves.

The outline of the paper is the following. Section 2 presents a second-order kinetic MHD solver in the two-dimensional case. Section 3 includes numerical test cases. Section 4 is the discussion and conclusion.

2. A GAS-KINETIC FLUX SPLITTING METHOD

In this section we will extend the gas-kinetic flux splitting method in [26] to a multidimensional case. For the sake of simplicity, we restrict our attention to two dimensions.

Assume that the computational domain is subdivided into quadrilaterals. For a numerical cell, such as A_{ij} in Fig. 1, the bounding surfaces ∂A_{ij} consist of four boundary elements S_k $(k = 1, 2, 3, 4)$, and $\mathbf{n}_k$ denotes its outward unit normal direction. The integration of Eq. (1.1) over the control volume A_{ij} gives the finite volume scheme

$$\frac{\partial}{\partial t}\iint_{A_{ij}} U\, dV + \sum_{k=1}^{4} F_{\mathbf{n}_k}(U(S_k))|S_k| = 0, \tag{2.1}$$

where the conservative variables $U = [\rho, \rho u_x, \rho u_y, \rho u_z, B_x, B_y, B_z, E]^T$, and the flux function $F_{\mathbf{n}_k}(U)$ across a cell interface in the normal $\mathbf{n}_k$-direction is defined by

$$F_{\mathbf{n}_k}(U) = \begin{pmatrix} \rho u_{\mathbf{n}_k} \\ \rho u_x u_{\mathbf{n}_k} - B_x B_{\mathbf{n}_k} + \cos\alpha_k p_* \\ \rho u_y u_{\mathbf{n}_k} - B_y B_{\mathbf{n}_k} + \sin\alpha_k p_* \\ \rho u_z u_{\mathbf{n}_k} - B_z B_{\mathbf{n}_k} \\ \sin\alpha_k \left(B_{\mathbf{n}_k} u_{\mathbf{t}_k} - B_{\mathbf{t}_k} u_{\mathbf{n}_k}\right) \\ \cos\alpha_k \left(B_{\mathbf{t}_k} u_{\mathbf{n}_k} - B_{\mathbf{n}_k} u_{\mathbf{t}_k}\right) \\ B_z u_{\mathbf{n}_k} - B_{\mathbf{n}_k} u_z \\ u_{\mathbf{n}_k}(E + p_*) - B_{\mathbf{n}_k}\left(u_{\mathbf{n}_k} B_{\mathbf{n}_k} + u_{\mathbf{t}_k} B_{\mathbf{t}_k} + u_z B_z\right) \end{pmatrix}. \tag{2.2}$$

Here p_* is the total pressure with the value $p_* = p + \frac{1}{2}(B_{\mathbf{n}_k}^2 + B_{\mathbf{t}_k}^2 + B_z^2)$; α_k is the angle

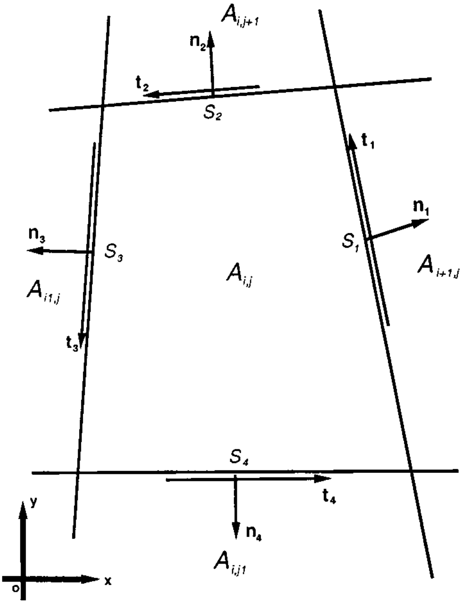

FIG. 1. Two-dimensional computational cell $A_{i,j}$.

between the normal direction $\mathbf{n}_k$ and the x-coordinate (measured in the anti-clockwise direction). In the above equations, $u_{\mathbf{n}_k}$, $u_{\mathbf{t}_k}$, $B_{\mathbf{n}_k}$, and $B_{\mathbf{t}_k}$ denote the components of the velocity and the magnetic field in the $\mathbf{n}_k$- and $\mathbf{t}_k$-directions; i.e.,

$$\begin{aligned} u_{\mathbf{n}_k} &= \cos\alpha_k u_x + \sin\alpha_k u_y, \quad & u_{\mathbf{t}_k} &= -\sin\alpha_k u_x + \cos\alpha_k u_y, \\ B_{\mathbf{n}_k} &= \cos\alpha_k B_x + \sin\alpha_k B_y, & B_{\mathbf{t}_k} &= -\sin\alpha_k B_x + \cos\alpha_k B_y. \end{aligned}$$

The numerical discretization of the two-dimensional ideal MHD equations (2.1) has become the evaluation of the local one-dimensional macroscopic flux function $F_{\mathbf{n}_k}$ through each boundary element. Based on the gas-kinetic theory, the flux is associated with the particle transport across a cell interface. For the one-dimensional flow, such as in the n-direction, the normal component of the particle velocity, such as v_n, is important in the determination of the flux function across this cell interface. Other quantities can be considered as passive scalars, which are transported with the n-direction particle motion. Since particles are randomly distributed around an average velocity, these moving particles in the n-direction can be favorably described by a Maxwell–Boltzmann distribution function,

$$g = \rho\left(\frac{\lambda}{\pi}\right)^{1/2} e^{-\lambda(v_n-u_n)^2}, \tag{2.3}$$

where u_n is the average fluid velocity in the n-direction, v_n is the individual particle velocity in the same direction, and λ is the normalization factor of the distribution of random velocity, which is related to the local temperature of the gas flow. For the MHD equations (1.1) with $U = [\rho, \rho u_x, \rho u_y, \rho u_z, B_x, B_y, B_z, E]^T$, both the gas and the magnetic field contribute to the total pressure p_*, and the total internal energy is a combination of gas and magnetic energy. Since the pressure is related to the integration of the particle distribution function g,

$$\int_{-\infty}^{\infty} (v_n - u_n)^2 g\, dv_n = \frac{\rho}{2\lambda}, \tag{2.4}$$

the value of λ in Eq. (2.3) is uniquely determined by $\lambda = \rho/2p_*$.

After determining λ, we can split the particles into two groups in the n-direction according to $v_n > 0$ and $v_n < 0$. As a result, the MHD flux function through a cell interface in the normal direction becomes $F_{\mathbf{n}_k}(U) = F^+_{\mathbf{n}_k}(U) + F^-_{\mathbf{n}_k}(U)$ ($k = 1, 2, 3$, or 4), where the positive and negative parts are

$$F^{\pm}_{\mathbf{n}_k}(U) = \begin{pmatrix} \rho \\ \rho u_x \\ \rho u_y \\ \rho u_z \\ -\sin\alpha_k B_{\mathbf{t}_k} \\ \cos\alpha_k B_{\mathbf{t}_k} \\ B_z \\ E + \frac{1}{2} p_0 \end{pmatrix} \left\langle v^1_{\mathbf{n}_k} \right\rangle_{\pm} + \begin{pmatrix} 0 \\ \cos\alpha_k p_* - B_x B_{\mathbf{n}_k} \\ \sin\alpha_k p_* - B_y B_{\mathbf{n}_k} \\ -B_z B_{\mathbf{n}_k} \\ \sin\alpha_k B_{\mathbf{n}_k} u_{\mathbf{t}_k} \\ -\cos\alpha_k B_{\mathbf{n}_k} u_{\mathbf{t}_k} \\ -B_{\mathbf{n}_k} u_z \\ -B_{\mathbf{n}_k}\left(B_{\mathbf{t}_k} u_{\mathbf{t}_k} + B_z u_z\right) + \frac{1}{2} p_0 u_{\mathbf{n}_k} \end{pmatrix} \left\langle v^0_{\mathbf{n}_k} \right\rangle_{\pm}. \tag{2.5}$$

Here $p_0 = p_* - B^2_{\mathbf{n}_k}$. In the above formulations, the moments $\langle v^0_{\mathbf{n}_k}\rangle_\pm$ and $\langle v^1_{\mathbf{n}_k}\rangle_\pm$ are defined by

$$\left\langle v^0_{\mathbf{n}_k}\right\rangle_\pm = \frac{1}{2}\,\mathrm{erfc}\left(\mp\sqrt{\lambda}u_{\mathbf{n}_k}\right)$$

and

$$\left\langle v^1_{\mathbf{n}_k}\right\rangle_\pm = u_{\mathbf{n}_k}\left\langle v^0_{\mathbf{n}_k}\right\rangle_\pm \pm \frac{1}{2\sqrt{\lambda\pi}}e^{-\lambda u^2_{\mathbf{n}_k}}.$$

As a result, the splitting flux function for the MHD equations at a cell interface, such as S_1 in Fig. 1, becomes

$$\left(F^{\mathrm{f}}_{\mathbf{n}_1}\right)_{i+1/2,j} = F^+_{\mathbf{n}_1}(U_{i,j}) + F^-_{\mathbf{n}_1}(U_{i+1,j}), \tag{2.6}$$

where "f" is used to denote the above free transport model. The above MHD flux splitting formulation goes back to the method developed by Croisille *et al.* in the one-dimensional case [6]. This KFVS-type MHD method is very robust, but overdiffusive, especially in the case with coarse mesh. To reduce the numerical dissipation, Xu [26] implemented a particle collisional mechanism in the above flux transporting process. The idea is to obtain an equilibrium state $U^{\mathrm{e}}_{\mathbf{n}_k}$ at the cell interface by combining the left and right moving beams and use this state to get an equilibrium flux function $F^{\mathrm{e}}_{\mathbf{n}_k}(U^{\mathrm{e}}_{\mathbf{n}_k})$ through the flux definition $F_{\mathbf{n}_k}(U(S_k))$ in Eq. (2.2). The equilibrium state at the cell interface, such as S_1, can be constructed as

$$\begin{aligned}\left(U^{\mathrm{e}}_{\mathbf{n}_1}\right)_{i+1/2,j} &= \left[\rho, \rho u_{\mathbf{n}_1}, \rho u_{\mathbf{t}_1}, \rho u_z, B_{\mathbf{n}_1}, B_{\mathbf{t}_1}, B_z, E\right]^T_{i+1/2,j}\\ &= U^+_{\mathbf{n}_1}(U_{i,j}) + U^-_{\mathbf{n}_1}(U_{i+1,j}),\end{aligned}$$

where

$$U^\pm_{\mathbf{n}_1}(U) = \begin{pmatrix} 0\\ \rho\\ 0\\ 0\\ 0\\ 0\\ 0\\ \frac{1}{2}\rho u_{\mathbf{n}_1}\end{pmatrix}\left\langle v^1_{\mathbf{n}_1}\right\rangle_\pm + \begin{pmatrix} \rho\\ 0\\ \rho u_{\mathbf{t}_1}\\ \rho u_z\\ B_{\mathbf{n}_1}\\ B_{\mathbf{t}_1}\\ B_z\\ E-\frac{1}{2}\rho u^2_{\mathbf{n}_1}\end{pmatrix}\left\langle v^0_{\mathbf{n}_1}\right\rangle_\pm. \tag{2.7}$$

Then, the final flux function across the cell interface S_1 is given by

$$\left(F_{\mathbf{n}_1}\right)_{i+1/2,j} = (1-\eta)\left(F^{\mathrm{e}}_{\mathbf{n}_1}\right)_{i+1/2,j} + \eta\left(F^{\mathrm{f}}_{\mathbf{n}_1}\right)_{i+1/2,j}, \tag{2.8}$$

where η is an adaptive parameter between [0, 1], which takes a constant 0.7 in all test cases of the current paper. Physically, η should be an adaptive parameter related to the real flow situation. For example, in the strong shock region, it must have a large value to account for the nonequilibrium property. The design of an optimum η related to the flow distribution is still an open question.

Now the semi-discrete finite difference version of the gas-kinetic scheme (2.1) becomes

$$\begin{aligned}\frac{dU_{i,j}(t)}{dt} = -\frac{1}{\Delta V}\Big(&\big(F_{\mathbf{n}_1}\big)_{i+1/2,j}|S_1| + \big(F_{\mathbf{n}_3}\big)_{i-1/2,j}|S_3| \\ &+ \big(F_{\mathbf{n}_2}\big)_{i,j+1/2}|S_2| + \big(F_{\mathbf{n}_4}\big)_{i,j-1/2}|S_4|\Big),\end{aligned} \tag{2.9}$$

where $F_{\mathbf{n}_k}$ denotes the fluxes across each boundary element in the normal direction and is defined in (2.8). Here, ΔV is the area of the quadrilateral A_{ij}. The above scheme is only first-order accurate in space. To improve the accuracy of the scheme, the initial reconstruction technique must be applied to interpolate the cell averaged variables, i.e., $U_{i,j}$. For example, a linear function,

$$\begin{aligned}\bar{U}_{i,j}(x,y) &= U_{i,j} + (U_x)_{i,j}(x - x_{i,j}) + (U_y)_{i,j}(y - y_{i,j}),\\ &\text{for } (x,y) \in \big[x_{i-1/2,j}, x_{i+1/2,j}\big] \times \big[y_{i,j-1/2}, y_{i,j+1/2}\big],\end{aligned} \tag{2.10}$$

can be constructed to approximate the cell averaged variables $U_{i,j}$ at the beginning of each time step, where $(U_x)_{i,j}$ and $(U_y)_{i,j}$ are the approximate slopes in the x- and y-directions inside the control volume A_{ij}. To avoid oscillations in the reconstructed data, the slope of U, such as in the x-direction, is obtained through the van Leer limiter,

$$(U_x)_{i,j} = (\mathrm{sgn}(s^+_{i,j}) + \mathrm{sgn}(s^-_{i,j}))\frac{|s^+_{i,j}||s^-_{i,j}|}{|s^+_{i,j}| + |s^-_{i,j}|}, \tag{2.11}$$

where sgn is the sign function, and

$$s^+_{i,j} = \big(U^n_{i+1,j} - U^n_{i,j}\big)\big/(x_{i+1,j} - x_{i,j}), \quad s^-_{i,j} = \big(U^n_{i,j} - U^n_{i-1,j}\big)\big/(x_{i,j} - x_{i-1,j}). \tag{2.12}$$

Similarly, $(U_y)_{i,j}$ can be constructed. In the current paper, the interpolation is imposed on the conservative variables directly, which is different from those schemes based on the characteristic waves decomposition [2].

Based on the above limited linear reconstruction (2.10), a high spatial resolution kinetic MHD solver becomes

$$\begin{aligned}&\frac{dU_{i,j}(t)}{dt}\\ &= -\frac{1}{\Delta V}\Big(\big(F_{\mathbf{n}_1}\big)_{i+1/2,j}\big(\tilde{U}_{i+1/2,j}, \hat{U}_{i+1/2,j}\big)|S_1| + \big(F_{\mathbf{n}_3}\big)_{i-1/2,j}\big(\tilde{U}_{i-1/2,j}, \hat{U}_{i-1/2,j}\big)|S_3| \\ &\quad + \big(F_{\mathbf{n}_2}\big)_{i,j+1/2}\big(\tilde{U}_{i,j+1/2}, \hat{U}_{i,j+1/2}\big)|S_2| + \big(F_{\mathbf{n}_4}\big)_{i,j-1/2}\big(\tilde{U}_{i,j-1/2}, \hat{U}_{i,j-1/2}\big)|S_4|\Big),\end{aligned} \tag{2.13}$$

where the flow variables next to the cell interface are

$$\tilde{U}_{i+1/2,j} = \bar{U}_{i,j}\big(x_{i+1/2,j}, y_{i+1/2,j}\big), \quad \hat{U}_{i+1/2,j} = \bar{U}_{i+1,j}\big(x_{i+1/2,j}, y_{i+1/2,j}\big),$$

and $\tilde{U}_{i,j+1/2}$ and $\hat{U}_{i,j+1/2}$ are defined similarly.

To improve the temporal accuracy, a second-order TVD Runge–Kutta scheme is used to solve Eq. (2.13) [18]. Denoting the right-hand side of (2.13) as $L(U)$, a second-order TVD Runge–Kutta scheme updates U through the following two stages:

$$\begin{aligned} U^{(1)} &= U^n + \Delta t L(U^n), \\ U^{n+1} &= \frac{1}{2}\left(U^n + U^{(1)} + \Delta t L\left(U^{(1)}\right)\right). \end{aligned}$$

3. NUMERICAL RESULTS

In this section, the van Leer limiter is used for the initial reconstruction of the conservative variables, and the coefficient η in the flux function (2.8) is taking a constant 0.7.

3.1. *Spherical Explosion [27]*

The computational domain of the explosion case is [0, 100] × [0, 100]. There is a high pressure region around the center with a radius $r = 10$. The initial density over the whole domain is 1, and the pressures inside and outside the central region are 100 and 1, respectively. Three different values of the initial magnetic field (B_x, B_y, B_z), (0, 0, 0), $(0, 5/\sqrt{\pi}, 0)$, and $(0, 50/\sqrt{\pi}, 0)$, are considered. In all three cases, γ is equal to 2.0 and a uniform mesh with 100 × 100 grid points is used.

When the problem is solved with zero initial magnetic field, the scheme goes back to the kinetic method for the compressible Euler equations. In this case, the fluid particles propagate symmetrically in the radial direction. The numerical solutions at $t = 3$ are shown in Fig. 2. When the strength of the initial magnetic field is increased to $B_y = 5/\sqrt{\pi}$, the shock front becomes slightly elongated in the direction of the magnetic field. The simulation results at time $t = 3$ are given in Fig. 3. If we continue to increase the strength of the magnetic field, due to the magnetic pressure, the fluid motion in the direction perpendicular to the magnetic field line will be severely suppressed. For example, with $B_y = 50/\sqrt{\pi}$, the explosion becomes highly anisotropic, as shown in Fig. 4. In comparison with the results in [27], the contours given by the kinetic scheme have fewer wiggles and smaller oscillations in all three cases.

3.2. *Orszag–Tang MHD Turbulence [15]*

This interesting problem was introduced by Orszag and Tang as a simple model to study MHD turbulence [15]. Similar problems were entensively studied by Dahlburg and Picone for the evolution of compressible vortex systems [7, 12]. Because of its complicated interaction between different waves generated as the vortex system evolving, the Orszag–Tang test has been used by many authors as a standard model to validate different numerical codes [9, 27]. The initial data for the current study are

$$\begin{aligned} &\rho(x, y, 0) = \gamma^2, \quad u_x = -\sin(y), \quad u_y = \sin(x), \\ &p(x, y, 0) = \gamma, \qquad B_x = -\sin(y), \quad B_y = \sin(2x), \end{aligned}$$

where $\gamma = 5/3$. The average magnitude of the velocity and the magnetic field are both about 1, and the initial average Mach number $M^2 = \rho_0|\mathbf{u}_0|/(\gamma p_0)$ becomes 1 as well.

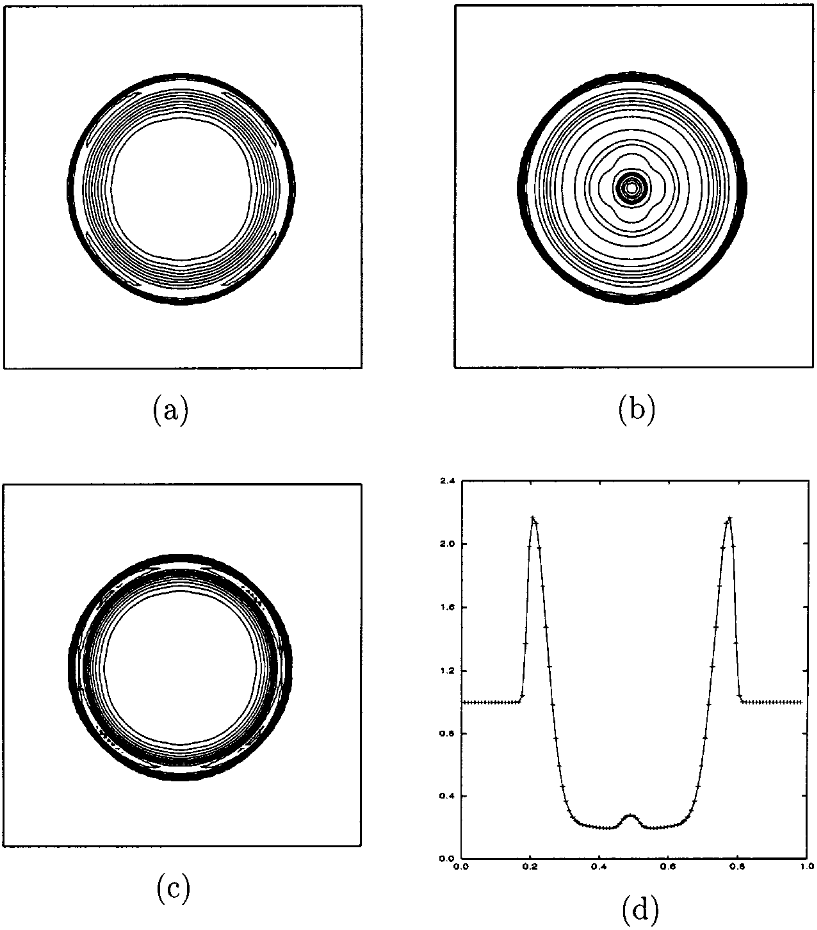

(a) (b) (c) (d)

FIG. 2. The solution of a spherical explosion case with initial magnetic field $B_y = 0$. The output time is at $t = 3.0$ and 100×100 grid points are used in the calculation. (a) Density; (b) gas pressure; (c) magnetic pressure; (d) density along $y = 0.5$.

The computation takes place on a domain of $[0, 2\pi] \times [0, 2\pi]$ with a uniform mesh of 192×192 grid points. The same cell size is used in the papers by Jiang and Wu [9] and Zachary *et al.* [27]. Periodic boundary conditions are imposed in both x- and y-directions. Figures 5–8 show the numerical results from the current kinetic scheme at the output times $t = 0.5, 2, 3$, and 8, where 20 contours are plotted in the density, gas pressure, magnetic pressure, and kinetic energy distributions. Figure 9 is the pressure distribution along a line at $y = 0.625\pi$, where the solid line is obtained with a refined mesh of 384×384 grid points. The perfect fitting of both curves in Fig. 9 illustrates that the kinetic scheme does give results convergent with those of the mesh refinement. The detailed pressure data with 192×192 grid points are listed in Table I for future reference. Figures 10–12 show the time evolution of the global magnetic energy, kinetic energy, and thermal energy. It is interesting to observe that the kinetic, magnetic, and thermal energies all approximate to some constants at later times in the MHD system, even though they are not precisely settling to the equal-partition distribution as commonly used in astrophysics. In comparison with the results from [9] and [27], the current results are closer to Jiang and Wu's numerical solutions, especially the pressure distribution in Fig. 9.

TABLE I

Pressure Distribution of the Orszag–Tang MHD Turbulence Simulation at Time $t = 3$ along a Cut at $y = 0.625\pi$

x	p	x	p	x	p	x	p	x	p
0.04960	2.537	0.7771	2.946	1.769	0.7065	3.522	3.105	4.845	0.7808
0.1157	2.655	0.8433	2.840	1.835	0.9467	3.588	3.136	5.010	0.8332
0.1819	2.772	0.9094	2.727	1.935	1.146	3.654	3.096	5.109	0.7523
0.2811	2.692	0.9755	2.650	2.133	1.307	3.786	2.853	5.175	0.5633
0.3472	2.647	1.108	2.602	2.398	1.363	3.919	2.637	5.241	0.5263
0.4134	3.238	1.339	2.640	2.662	1.388	4.018	2.599	5.473	0.5433
0.4795	2.776	1.472	2.652	2.861	1.430	4.150	2.642	5.704	0.6486
0.5126	2.679	1.505	2.616	2.993	1.554	4.282	2.749	6.002	0.9079
0.5456	2.726	1.571	1.958	3.059	1.696	4.316	2.386	6.068	1.037
0.6118	2.979	1.637	0.5440	3.191	2.247	4.349	1.002	6.134	1.526
0.6449	3.034	1.670	0.5289	3.323	2.754	4.382	0.6685	6.201	2.324
0.7110	3.007	1.703	0.5629	3.456	3.023	4.580	0.7003	6.267	2.590

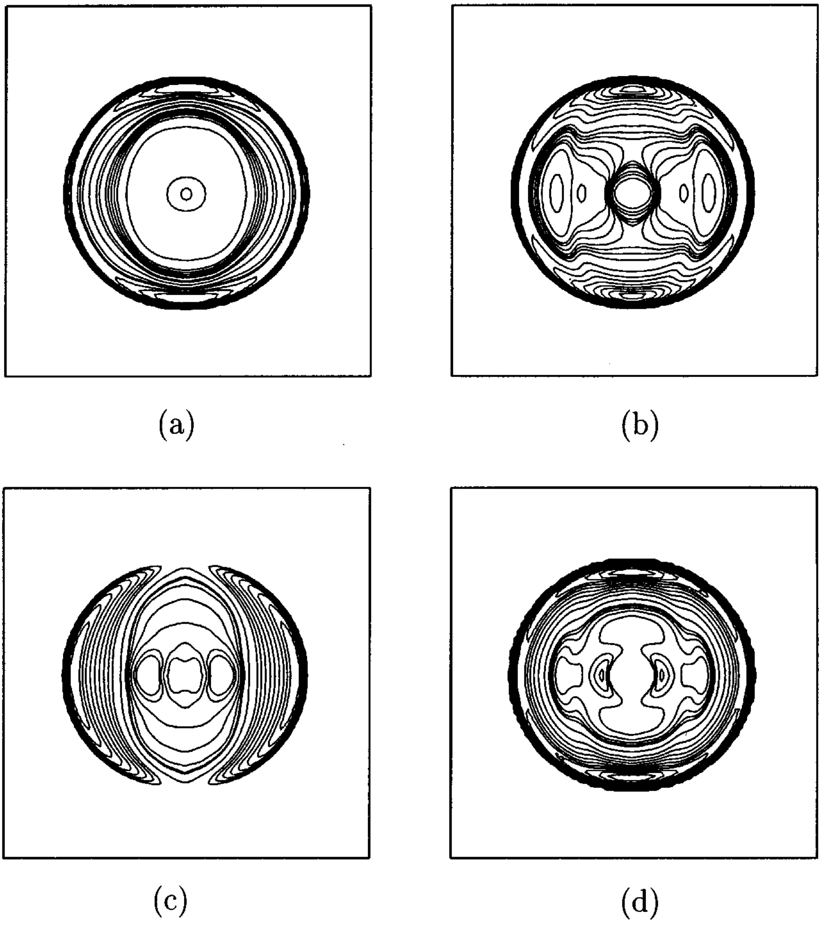

FIG. 3. The solution of a spherical explosion case with an initial field $B_y = 5/\sqrt{\pi}$. The output time is at $t = 3.0$. (a) Density; (b) gas pressure; (c) magnetic pressure; (d) kinetic energy.

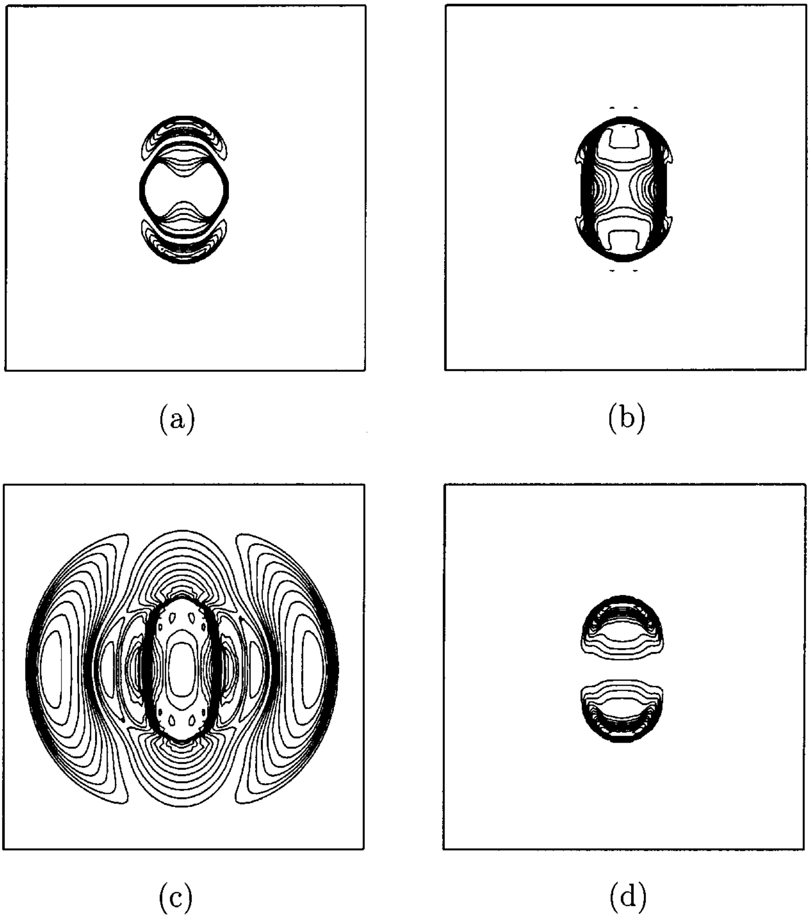

FIG. 4. The solution of a spherical explosion case with an initial field $B_y = 50/\sqrt{\pi}$. The output time is at $t = 1.05$. (a) Density; (b) gas pressure; (c) magnetic pressure; (d) kinetic energy.

3.3. *Kelvin–Helmholtz Instability [24]*

The Kelvin–Helmholtz instability arises when two superposed fluid flows have a relative velocity. It can be considered an important mechanism for momentum transfer at the Earth's magnetopause boundary, which separates the solar wind from the Earth's magnetosphere. Similarly to the calculations in [9], we consider both periodic and convective models, which are defined in terms of the x-direction boundary conditions.

The initial data of the periodic and convective models are given by $\rho = 1$, $u_x = (u_0/2)\tanh(y/a)$, $B_z = 0$, and $p = 0.5$, where a denotes the width of the velocity shear layer with the value of 1, $u_0 = 2$, and $\gamma = 2$. Initially, a small perturbation for the velocity field is imposed,

$$\tilde{u}_x = \begin{cases} -\tilde{u}_0 \sin(2\pi x/\lambda)/(1+y^2), & \text{if } x \in \left[-\frac{\lambda}{2}, \frac{\lambda}{2}\right], \\ 0, & \text{otherwise,} \end{cases}$$

where $\tilde{u}_0 = 0.008$ and $\lambda = 5\pi$ in the above perturbation. The computational domain used is

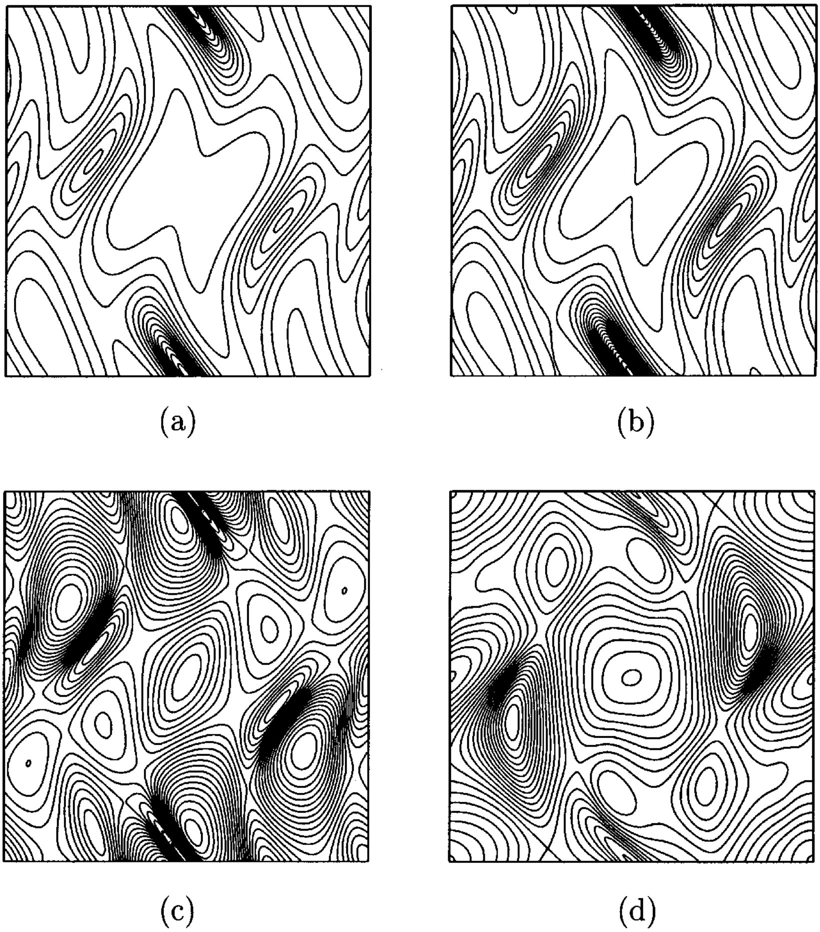

FIG. 5. The Orszag–Tang MHD turbulence problem with a uniform mesh of 192 × 192 grid points. The output time is $t = 0.5$: There are 20 contours for density, pressure, magnetic pressure, and kinetic energy. (a) Density; (b) gas pressure; (c) magnetic pressure; (d) kinetic energy.

$[-L/2, L/2] \times [-H, H]$, where $L = \lambda$ and $H = 10$ for the periodic case, and $L = 11\lambda$ and $H = 20$ for the convective case. In both cases, the outflow boundary conditions are applied at the top and bottom boundaries. In the x-direction, the periodic boundary condition is used for the periodic model and the outflow boundary condition is used for the convective case. With the consideration of initial velocity distribution, Jiang and Wu used an adaptive mesh in their calculations, where the smallest cell size used is $\Delta y = 0.1275$ for the convective model, and $\Delta y = 0.103448$ and 0.0507786 for the two periodic cases. In our calculations, a uniform mesh with $\Delta y = 0.1$ is used in all cases. The use of a fine mesh to resolve the initial velocity field is necessary in the current example. Otherwise, if a large cell size around $y = 0$ is used, the initial velocity distribution will be erroneously represented. Figures 13–15 show contours of the density and pressure obtained by the current method at different output times for the periodic and convective cases. Figure 16 presents the time evolution of the total transverse kinetic energy $\frac{1}{2}\int \rho u_y^2 \, dx \, dy$ for the periodic and convective systems. Our numerical results are very close to those obtained using fifth-order WENO methods [9].

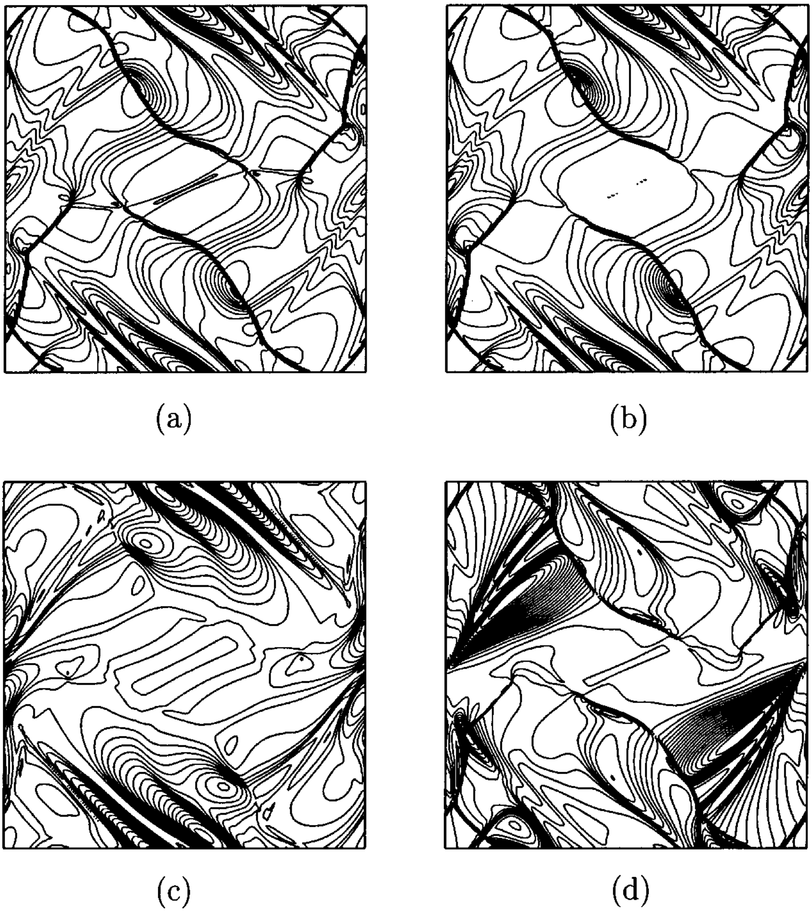

FIG. 6. The Orszag–Tang MHD turbulence problem at output time $t = 2$. (a) Density; (b) gas pressure; (c) magnetic pressure; (d) kinetic energy.

To further demonstrate the accuracy of the kinetic scheme, we have calculated the Kelvin–Helmholtz instability with different mesh sizes. Table II shows a comparison between the kinetic schemes with $\eta = 0.7$ and $\eta = 1.0$ for the above periodic model with a uniform grid in both x- and y-directions over the computational domain $[-\frac{5\pi}{2}, \frac{5\pi}{2}] \times [-10, 10]$. For each run, we list the maximum transverse kinetic energy attained and the time when it occurs. In comparison with the results presented in Table V of [9], the kinetic scheme could give

TABLE II
The Maximum Total Transverse Kinetic Energy E_k of the Periodic Kelvin–Helmholtz Instability Case on a Mesh Refinement Study

	BGK scheme ($\eta = 0.7$)		KFVS scheme ($\eta = 1.$)	
Grid	E_k	Time	E_k	Time
50 × 100	3.1288	88.2061	2.3648	93.3091
100 × 200	3.8040	78.7819	3.7261	79.8388
200 × 400	3.8275	77.4621	3.8292	77.5723

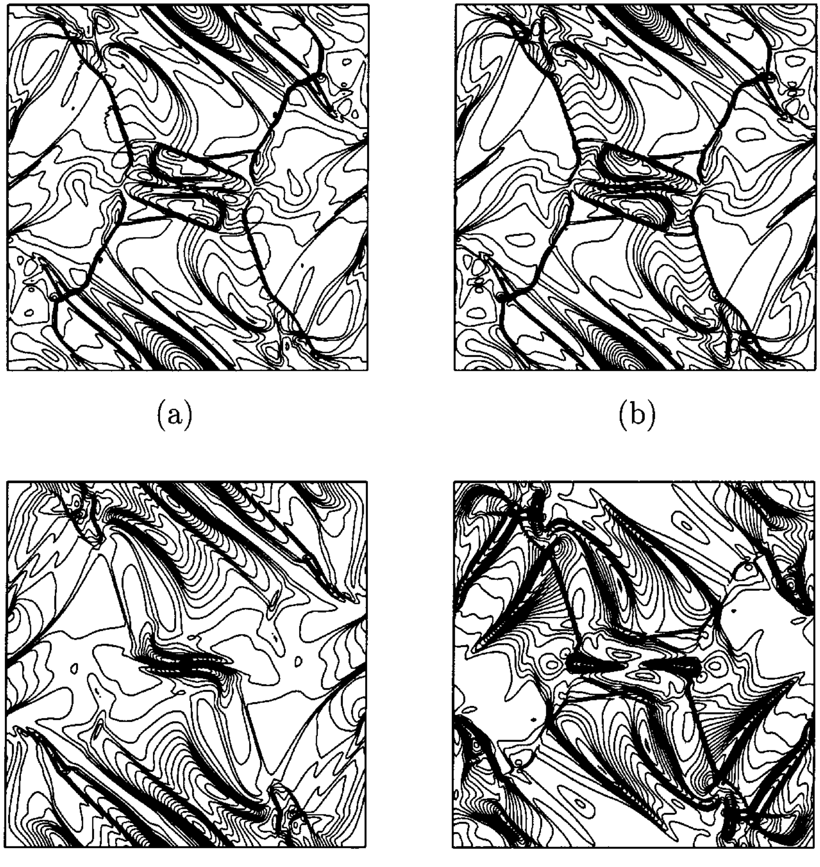

FIG. 7. The Orszag–Tang MHD turbulence problem at output time $t = 3$. (a) Density; (b) gas pressure; (c) magnetic pressure; (d) kinetic energy.

a higher converged transverse kinetic energy E_k, i.e., $E_k = 3.827$ instead of $E_k = 3.703$ of fifth-order ENO method [9], and our results are much better than those obtained from other second-order methods [9]. Also, the difference in numerical dissipation between the schemes with collisional $\eta = 0.7$ and free transport $\eta = 1.0$ models can be clearly observed, especially in the coarse mesh case with 50×100 grid points. Fortunately, for both kinetic models the numerical results converge with the mesh refinements.

4. DISCUSSION AND CONCLUSION

In this paper we have extended the gas-kinetic theory based flux splitting method [26] to the multidimensional MHD calculations. The numerical flux function is constructed with the consideration of particle transport across the cell interfaces and particle “collisions” are implemented in the transport process to reduce the numerical dissipation. The parameter η, which determines the weights between the free transport and equilibrium fluxes in Eq. (2.8), takes a constant value in the current study. Although we have restricted our attention to the two-dimensional case in the current paper, the extension of the current method to three

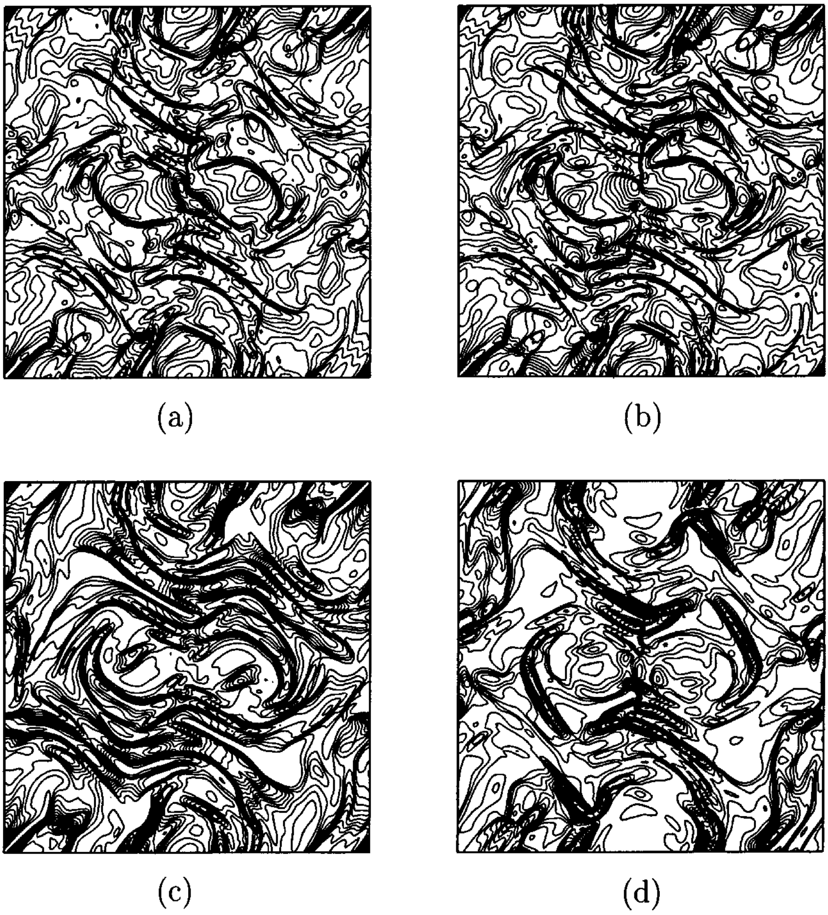

FIG. 8. The Orszag–Tang MHD turbulence problem at output time $t = 8$. (a) Density; (b) gas pressure; (c) magnetic pressure; (d) kinetic energy.

dimensions using the directional splitting method is straightforward. Second-order spatial resolution has been obtained in the current gas-kinetic approach with the implementation of a MUSCL-type interpolation technique, and the temporal resolution is improved by the use of the Runge–Kutta time-stepping method. The current scheme has been successfully applied to the spherical explosion, Kelvin–Helmholtz instability, and Orszag–Tang MHD turbulence test cases. In the near future, we are going to apply the 3D kinetic method to the study of the interaction of the solar wind with a magnetized planet [13]. Finally, we give several remarks about the current MHD solver.

(1) The initial reconstruction can be applied to the conservative or primitive variables. Due to the different amounts of dissipation introduced in the above approaches, the results of the MHD system depend more sensitively on the limiters and the variables used than the results of the Euler equations, especially in the cases with strong magnetic field.

(2) Similarly to any other MHD solvers, to obtain accurate and stable solutions we have used a correction method to enforce the divergence-free condition $\nabla \cdot \mathbf{B} = 0$. It is possible to specifically design an update procedure for the magnetic field to satisfy the divergence-free condition automatically. However, with the consideration of the errors involved in the

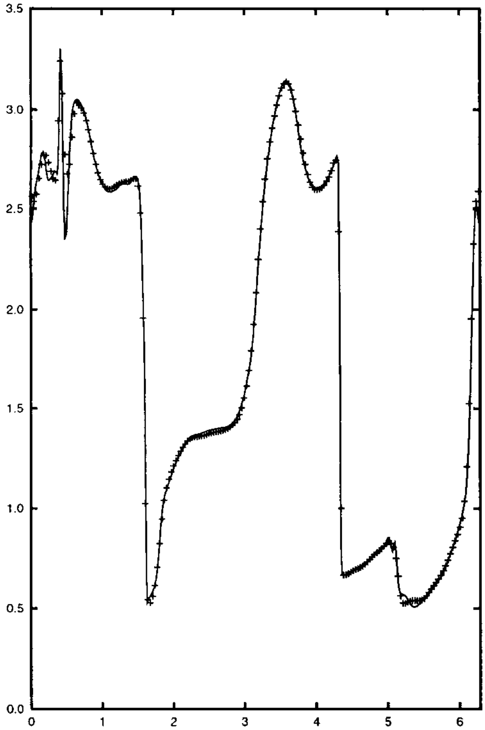

FIG. 9. The pressure distribution along the line $y = 0.625\pi$ for the Orszag–Tang MHD turbulence problem at output time $t = 3$, where the + represents the result with 192 × 192 grid points calculation, and the solid line is obtained with a fine mesh of 384 × 384 grid points. The data from 192 × 192 grid points calculation are listed in Table I for future references.

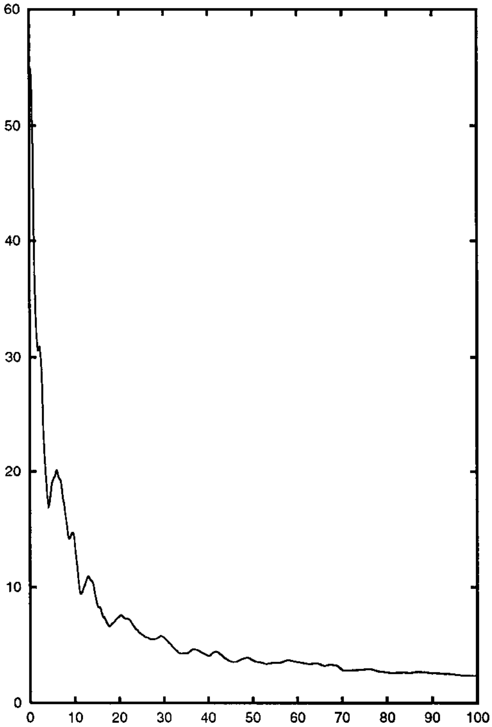

FIG. 10. The time evolution of global kinetic energy for the Orszag–Tang MHD turbulence problem. The calculation has been done up to time $t = 100.0$ with 192 × 192 grid points.

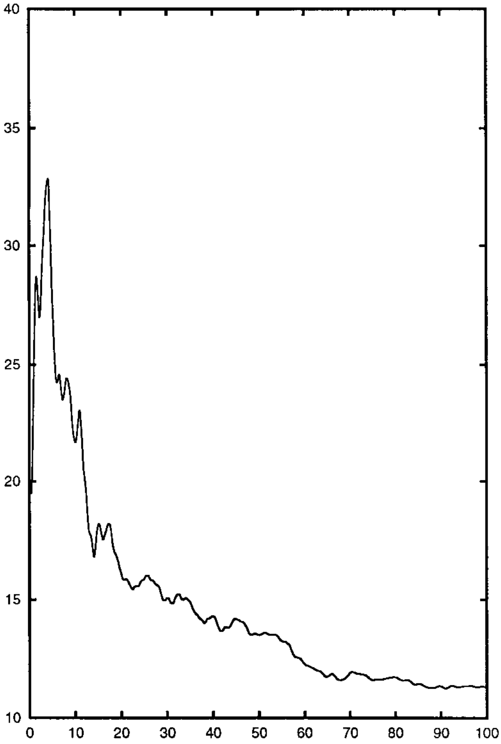

FIG. 11. The time evolution of global magnetic energy for the Orszag–Tang MHD turbulence problem.

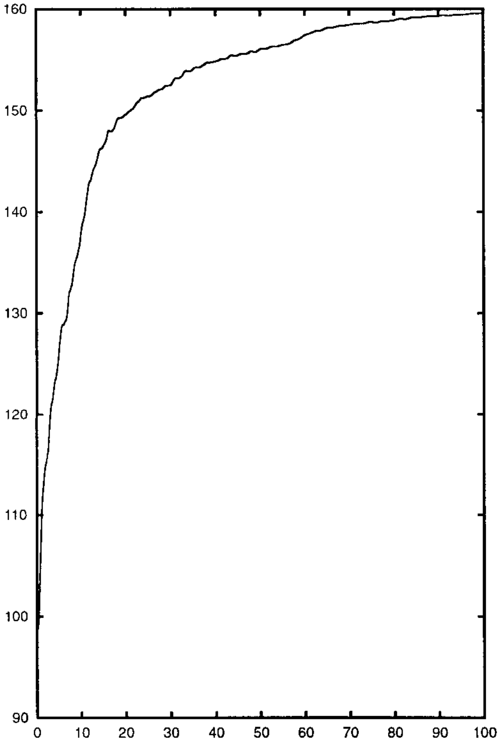

FIG. 12. The time evolution of global thermal energy for the Orszag–Tang MHD turbulence problem.

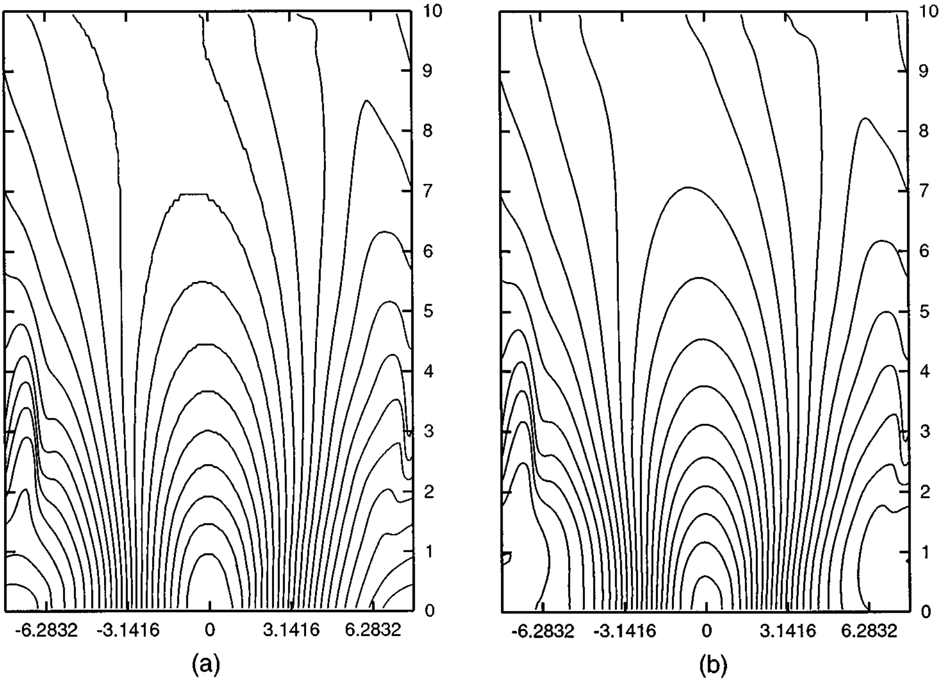

FIG. 13. The Kelvin–Helmholtz instability in the periodic case. The output time is $t = 144$. A uniform mesh with 200×200 grid points is used and 20 contours are plotted. (a) Density; (b) pressure.

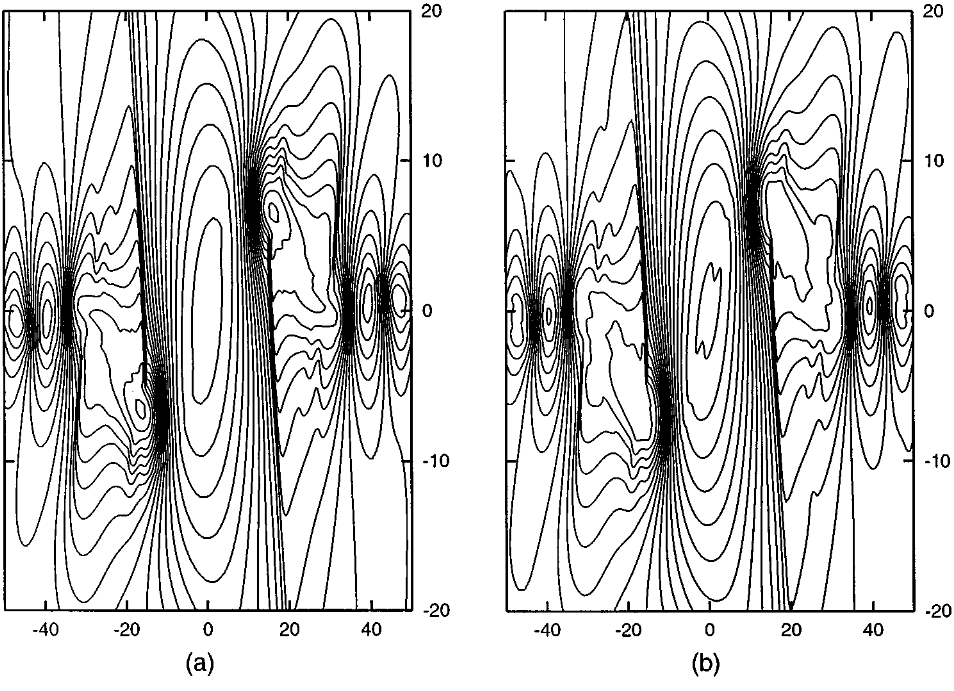

FIG. 14. The Kelvin–Helmholtz instability in the convective case at output time $t = 120$. A uniform mesh with 528×400 grid points is used and 20 contours are plotted. The current calculation is on the whole computational domain of $[-L/2, L/2] \times [-H, H]$ instead of the half domain $[-L/2, L/2] \times [0, H]$ used in Jiang and Wu's paper [9]. (a) Density; (b) pressure.

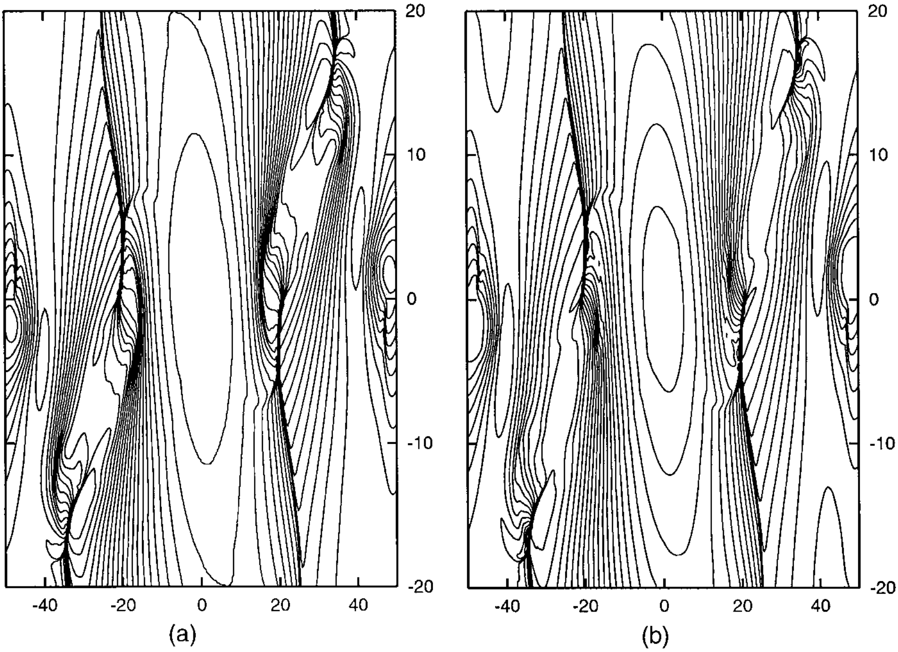

FIG. 15. The Kelvin–Helmholtz instability in the convective case at output time $t = 145$. (a) Density; (b) pressure.

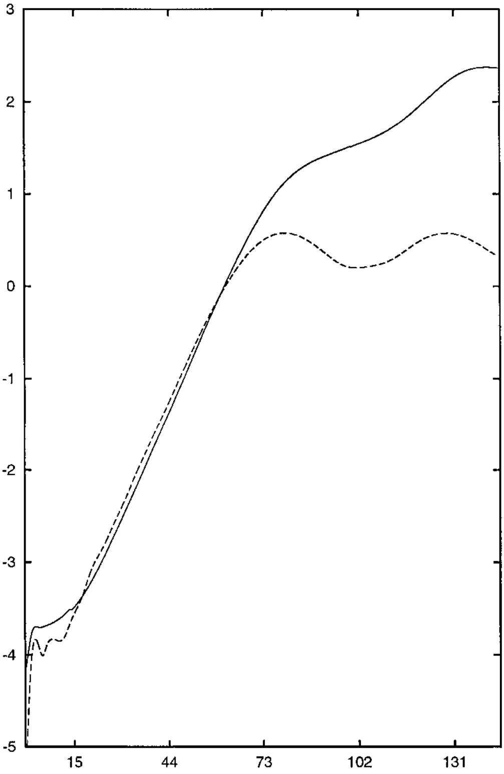

FIG. 16. The time evolution of the total transverse kinetic energy $\log(\frac{1}{2}\int \rho u_y^2\, dx\, dy)$ for the Kelvin–Helmholtz instability case. The solid and dashed curves represent the results of the convective and periodic cases, respectively.

process of reconstruction, directional splitting, and the flux approximation, the assessment of the real improvement in the numerical solutions from the automatical satisfaction of divergence-free condition will be difficult. But it is still interesting to develop such a MHD solver.

(3) Because the kinetic method avoids the complicated wave decomposition procedure implemented in most approximate Riemann solvers, the kinetic method is very efficient in comparison with other MHD solvers. As shown in this paper, the accuracy of the kinetic scheme is comparable to that of other high-resolution methods. Also, no entropy fix is needed to obtain a physically realizable solution in the gas-kinetic approach. At the end, it should be emphasized that the current method has only second-order accuracy. How to extend the kinetic scheme to a higher order one, which is required in turbulence simulation, is still an open question.

ACKNOWLEDGMENTS

We thank Professor C. C. Wu for helpful discussion about MHD waves and the numerical implementation of the Kelvin–Helmholtz instability problem. H. Z. Tang is supported by the National Natural Science Foundation of China and the Laboratory of Computational Physics of Beijing IAPCM. K. Xu is supported by the Hong Kong Research Grant Council through Grants HKUST6132/00P and DAG98/99.SC22.

REFERENCES

1. N. Aslan, MHD-A: A fluctuation splitting wave model for planar magnetohydrodynamics, *J. Comput. Phys.* **153**, 437 (1999).
2. D. S. Balsara, Total variation diminishing scheme for adiabatic and isothermal magnetohydrodynamics, *Astrophys. J. Suppl.* **116**, 133 (1998).
3. D. S. Balsara and D. S. Spicer, A staggered mesh algorithm using high order Gudunov fluxes to ensure solenoidal magnetic fields in magnetohydrodynamics simulations, *J. Comput. Phys.* **149**, 270 (1999).
4. J. U. Brackbill and D. C. Barnes, The effect of nonzero div **B** on the numerical solution of the magnetohydrodynamic equations, *J. Comput. Phys.* **35**, 426 (1980).
5. M. Brio and C. C. Wu, An upwind differencing schemes scheme for the equations of ideal magnetohydrodynamic equations, *J. Comput. Phys.* **75**, 400 (1988).
6. J.-P. Croisille, R. Khanfir, and G. Chanteur, Numerical simulation of the MHD equations by a kinetic-type method, *J. Sci. Comput.* **18**, 481 (1995).
7. R. B. Dahlburg and J. M. Picone, Evolution of the Orszag–Tang vortex system in a compressible medium. I. Initial average subsonic flow, *Phys. Fluids B* **1**, 2153 (1989).
8. W. Dai and P. R. Woodward, A high-order Godunov-type scheme for shock interactions in ideal magnetohydrodynamics, *SIAM J. Sci. Comput.* **18**, 957 (1997).
9. G. S. Jiang and C. C. Wu, A high-order WENO finite difference scheme for the equation of ideal magnetohydrodynamics, *J. Comput. Phys.* **150**, 561 (1999).
10. O. S. Jones, U. Shumlak, and D. S. Eberhardt, An implicit scheme for nonideal magnetohydrodynamics, *J. Comput. Phys.* **130**, 231 (1997).
11. R. S. Myong and P. L. Roe, On Godunov-type schemes for magnetohydrodynamics. I. A model system, *J. Comput. Phys.* **147**, 545 (1998).
12. J. M. Picone and R. B. Dahlburg, Evolution of the Orszag–Tang vortex system in a compressible medium. II. Supersonic flow, *Phys. Fluids B* **3**, 29 (1991).
13. K. G. Powell, P. Roe, T. Linde, T. I. Gombosi, and D. L. DeZeeuw, A solution-adaptive upwind scheme for ideal magnetohydrodynamics, *J. Comput. Phys.* **154**, 284 (1999).
14. D. I. Pullin, Direct simulation methods for compressible inviscid ideal gas flow, *J. Comput. Phys.* **34**, 231 (1980).

15. S. A. Orszag and C. M. Tang, Small-scale structure of two-dimensional magnetohydrodynamic turbulence, *J. Fluid. Mech.* **90**, 129 (1979).
16. D. Ryu, T. W. Jones, and A. Frank, Numerical magnetohydrodynamics in astrophysics: Algorithm and tests for multidimensional flow, *Astrophy. J.* **452**, 785 (1995).
17. D. D. Schnack, I. Lottati, Z. Mikie, and P. Satyanarayana, A finite-volume algorithm for three-dimensional magnetohydrodynamics on an unstructured adaptive grid in axially symmetric geometry, *J. Comput. Phys.* **140**, 71 (1998).
18. C. W. Shu, Total-variation-diminishing time discretizations, *SIAM J. Sci. Stat. Comput.* **9**, 1073 (1988).
19. J. L. Steger and R. F. Warming, Flux-vector splitting of the inviscid gas-dynamic equations with applications to finite difference schemes, *J. Comput. Phys.* **40**, 263 (1981).
20. H. R. Strauss and D. W. Longcope, An adaptive finite element method for magnetohydrodynamics, *J. Comput. Phys.* **147**, 318 (1998).
21. T. Tanaka, Finite volume TVD scheme on an unstructured grid system for three-dimensional MHD simulations of inhomogeneous systems including strong background potential field, *J. Comput. Phys.* **111**, 81 (1995).
22. B. van Leer, Towards the ultimate conservative difference schemes. V. A second-order sequel to Godunov's method, *J. Comput. Phys.* **32**, 101 (1979).
23. B. van Leer, *Flux-Vector Splitting for the Euler Equations*, ICASE Report 82-30 (1982).
24. C. C. Wu, Kelvin–Helmholtz instability at the magnetopause boundary, *J. Geophys. Res.* **91**, 3042 (1986).
25. K. Xu, *Gas-Kinetic Schemes for Unsteady Compressible Flow Simulations*, 29th CFD Lecture Series 1998-03 (von Karman Institute for Fluid Dynamics, 1998).
26. K. Xu, Gas-kinetic theory based flux splitting method for ideal magnetohydrodynamics, *J. Comput. Phys.* **153**, 334 (1999).
27. A. Zachary, A. Malagoli, and P. Colella, A high-order Godunov method for multidimensional ideal magnetohydrodynamics, *SIAM J. Sci. Comput.* **15**, 263 (1994).